The nature and suppression strategies of interfacial reactions in all-solid-state batteries†

Fucheng Ren,[a] Ziteng Liang,[b] Wengao Zhao,[c] Wenhua Zuo,[d] Min Lin,[b] Yuqi Wu,[a] Xuerui Yang,[a] Zhengliang Gong *[a] and Yong Yang *[ab]

Solid-state Li batteries are promising energy storage devices owing to their high safety and high theoretical energy density. However, the serious interfacial reaction between solid state electrolytes and cathodes deteriorates the battery performance, impeding the realization of long-term cyclability. The buried nature of the interphase layer presents a significant challenge in achieving a comprehensive understanding of the underlying interfacial reaction mechanisms. Herein, we systematically explore the interfacial reaction evolutions and interphase compositions and electronic properties between the popular oxide cathodes and sulfide solid electrolytes (SSEs). This includes analysis of the chemical and electrochemical reactions between cathodes/coatings and SSEs, as well as the electrochemical self-decomposition of SSEs by thermodynamic phase equilibrium analysis. We disclose that the driving force of the electrochemical reaction at the chemical potential of μ_{Li} is much stronger than that of the chemical reaction, which dominates the interfacial reaction. Preventing the formation of an electronically conductive interphase is crucial in inhibiting the continuous interfacial degradation during long-term cycling, which can be achieved through the optimized combination of cathodes and SSEs, as well as the introduction of functional coatings between them. Based on these findings, the percentage of molar fraction (f) of electronically conductive species in the formed interphase is proposed as a key factor for indicating the interfacial stability for the first time. Furthermore, we propose a specific high-throughput screening scheme to filter the functional coating materials by comprehensively evaluating their functionality. The tiered screening identifies 48 coating materials with optimal properties. The work highlights the significant roles of rational coupling of the cathodes and SSEs, and optimizing interfacial coating materials for solid-state batteries. It opens new avenues for engineering an interphase with improved interfacial compatibility to realize long-term cyclability.

Broader context

Solid-state Li batteries incorporated with inorganic solid electrolytes effectively improve the safety and energy density of batteries. However, the severe interface reaction between cathodes and sulfide solid electrolytes (SSEs) significantly degrades the cycling performance of batteries. Herein, we provide a comprehensive understanding of interfacial reaction mechanisms in sulfide-based composites. It is a general trend that the driving force of the electrochemical reaction between oxide cathodes and SSEs is much stronger than that of the chemical reaction, dominating the interfacial reaction; furthermore, plenty of binary transition metal sulfides as electronic conductors can be formed by chemical/electrochemical reactions, providing an electron conducting network for electrochemical reactions. The percentage of the molar fraction of electronically conductive species in all formed interphases is proposed for the first time which can effectively indicate the interfacial compatibility. Hence, decreasing the electronic conductivity of the interphase layer between cathodes/coatings and SSEs is crucial for realizing long-term cyclability of solid-state batteries.

[a] *College of Energy, Xiamen University, Xiamen, 361102, China. E-mail: zlgong@xmu.edu.cn*
[b] *State Key Laboratory for Physical Chemistry of Solid Surface, Department of Chemistry, College of Chemistry and Chemical Engineering, Xiamen University, Xiamen, 361005, China. E-mail: yyang@xmu.edu.cn*
[c] *Institute of Nanotechnology, Karlsruhe Institute of Technology (KIT), 76344 Eggenstein-Leopoldshafen, Germany*
[d] *Chemical Sciences and Engineering Division, Argonne National Laboratory, Lemont, IL, 60439, USA*

Introduction

Lithium-ion batteries have become an indispensable part of our life, and their applications range from consumer electronics to electric vehicles and large-scale energy storage. As intelligence and electrification continue to develop, the importance of batteries is increasing.[1] This places more stringent requirements on their

applications, such as higher safety, energy density, and long-term cycling stability. Conventional lithium-ion batteries that use liquid organic electrolytes are at risk of catching fire and leaking. Replacing the organic electrolyte with a solid inorganic electrolyte can effectively mitigate the aforementioned issues. By using solid electrolytes, an alkali metal can be used as an anode, which can significantly improve the energy density of the battery, thereby enabling the realization of solid-state lithium-ion batteries with improved safety, energy density, and long-term cycling stability. Great efforts have been made to develop solid inorganic fast ionic conductors which can be mainly categorized into four types including oxides,[2–4] sulfides,[5–7] halides,[8,9] and composite solid electrolytes.[10] Among them, sulfide solid electrolytes have attracted immense interest due to their high ionic conductivity, which is close to or even exceeds those of conventional liquid electrolytes ($\sigma_{Li^+} \sim 10$ mS cm^{-1}), *e.g.*, $Li_7P_3S_{11}$ (17 mS cm^{-1}),[11] $Li_{10}GeP_2S_{12}$ (12 mS cm^{-1}),[12] $Li_{9.54}Si_{1.74}P_{1.44}S_{11.7}Cl_{0.3}$ (25 mS cm^{-1}),[13] and Li_6PS_5Cl (1.9 mS cm^{-1}).[6]

Nevertheless, the exchange between a transition metal and P, as well as O and S anions, is thermodynamically favorable due to the difference in chemical potential between the cathode and the SSE at the interface.[14–17] The severe interfacial reactions between sulfide solid electrolytes and oxide cathodes lead to the formation of a thick interphase layer and an increase in the interfacial resistance, which reduce the battery performance and stability, and severely restrict the practical application of all-solid-state batteries (ASSBs). It was found that the Co diffusion depth can reach 50 nm at the LCO/Li_2S–P_2S_5 interface.[18] This transition metal diffusion degrades the surface structural integrity of the cathode, resulting in uneven stress distribution within the cathode particles, which intensifies the fragmentation of the cathode particles. These intricate interactions eventually lead to rapid capacity decay.[19] Furthermore, the performance of ASSBs varies greatly depending on the combination of a specific sulfide solid electrolyte (SSE) with different types of cathodes, as well as a specific cathode with different types of electrolytes. However, there is still a lack of in-depth understanding of interfacial chemistry and stability between the cathode and sulfide solid electrolytes, due to the buried nature of the interphase layer, which makes the experimental characterization of the interphase very challenging and common spectroscopic approaches often lack the required reliability. This significantly restricts the accurate selection of the optimal electrolyte for cathodes, leaving trial and error as the primary viable option in experiments. The lack of significant differences in SEM, XPS, and EDX results has limited the accurate selection of the optimal electrolyte for cathodes, leaving trial and error as the only viable option in experiments.[20–22] Therefore, understanding the intricate mechanisms of interfacial reactions and interphase layer formation is crucial for addressing the interfacial challenges in ASSBs to accelerate the realization of long-term cycling of ASSBs.

Oxide buffer layers such as $LiNbO_3$,[23–25] Li_4SiO_4,[26] Li_3PO_4,[27,28] $LiTaO_3$,[29] $LiAlO_2$,[30] Li_3BO_3,[31] *etc.*, can effectively improve the interfacial stability and reduce the interfacial resistance, achieving enhanced capacity retention and rate performance. Coatings are used to isolate the SSEs from the active material, and should be stable with both SSEs and cathodes. However, ASSBs with different coating materials exhibit diverse electrochemical performances. There is a lack of full understanding of the atomistic mechanism of the coating layers. Most ASSBs deliver a cycling life below/less than 500 cycles, which cannot satisfy the requirements of commercialization. The properties of the interphase layer formed between SSEs and cathode/coatings play a crucial role in determining the performance of all-solid-state batteries. If the interfacial reactions proceed continuously during cycling, it can lead to the thickening of the interphase layer and electrochemical performance degradation of the ASSBs. Most of the interphase layers are a mixed ionic and electronic conductor (MIEC), which are beneficial for the continuous electrochemical decomposition of the interphase, thus leading to poor capacity retention.[32] Therefore, an electron-insulating and ion conductive interphase layer is preferred. For example, benefiting from the passivation layer at both the anode and cathode sides, the Li/LiPON/LNMO ASSBs can sustain over 10 000 cycles with a high-capacity retention of 90%.[33]

Screening various coating materials and methods through experiments can be a time-consuming and expensive process, and it may be challenging to explore a wide range of operating conditions. High-throughput screening (HTS) is an effective strategy to develop new functional materials based on several specific properties.[34–36] Using the computational approach, several excellent works investigated the chemical stability of different interface systems and screened the potential coatings.[17,37–47] The reported HTS mainly considered the following aspects of coatings: electronic conductivity, phase and electrochemical stability, and reactivity with both the cathode and the electrolyte.[45,48–50] For ASSBs, ionic conductivity is an important criterion for coatings, but has often been neglected in the HTS, because of the high computation cost of ion conductivity using *ab initio* calculation.[51] In addition, coating layers and solid electrolytes are not entirely inert, as they can also undergo reactions that can affect the performance of batteries. Therefore, the electronic conductivity of the interphases formed between coatings and SSEs should also be carefully considered to avoid the formation of an MIEC interphase layer.

In this work, we systematically analyzed the possible interfacial reactions between the popular oxide cathodes and sulfide solid electrolytes (SSEs) at both fully/half-lithiated states in ASSBs by thermodynamic phase equilibrium analysis. Our findings reveal that the electrochemical reaction dominates the decomposition at the interface, with a driving force $\sim$3 times larger than that of the chemical reaction. The electronic conductivity of the interphase layer plays a critical role in the interfacial stability during electrochemical cycling. A large amount of transition metal sulfides (M_xS_y, M = transition metal) are formed by the interfacial reaction between cathodes and SSEs as electronic conductors. This greatly enhances the electronic conductivity of the interphase layer and aggravates the interfacial electrochemical reaction, resulting

in a thickening of the interphase layer and performance degradation. Based on these findings, we propose the percentage of molar fraction (f) of electronically conductive species in the formed interphases as a crucial factor for assessing interfacial stability. Furthermore, we proposed a specific high-throughput screening scheme to identify and filter the functional coatings for cathodes that can further enhance interfacial compatibility and Li-ion conductivity. We systematically take various aspects into account such as phase stability, electronic conductivity, and ionic conductivity (performed using CVAD and BVSE calculations), chemical stability with both SSEs and cathodes, and the electronic conductivity of the formed interphase layer. A diverse range of fast ion conductors, such as $LiTaSiO_4$, $Li_3Sc(BO_3)_2$, Li_3InCl_6, *etc.*, which exhibit high compatibility with both cathodes and SSEs, have been identified, validating the rationality and effectiveness of our screening scheme.

Results and discussion

Diverse interfaces and interfacial reactions in the composite cathode

Since the composite cathode is composed of a mixed cathode, electrolyte, and electronically conductive additives, it leads to the formation of multiple interfaces as illustrated in Fig. 1. The interfaces within the composite cathodes provide venues for various parasitic reactions, which can lead to an increase in interfacial resistance and the deterioration of cycling performance.[52,53] These interfacial reactions can be categorized into two aspects: chemical and electrochemical reactions. Electrochemical reactions occur at the interface of electronic conductors and ionic conductors. For example, the SSEs can be oxidized at electronically conductive additive/electrolyte and current collector/electrolyte interfaces during cycling, even if the SSEs are chemically inert with these two electronic conductors, due to the applied voltage (>4.2 V) exceeding the intrinsic stability window of SSEs (1.68–2.4 V) shown in Fig. S1 (ESI†). Fortunately, the phases formed by the oxidation of SSEs are electronically insulating, such as S, P_2S_7, *etc.* as listed in Table S1 (ESI†), which can effectively passivate the interfaces and inhibit the further decomposition of SSEs. Thus, the composite cathodes consisting of SSEs as active materials and electronically conductive additives can be cycled, although they exhibit severe capacity decay.[54 57]

At the cathode/electrolyte interface, the coexistence of chemical and electrochemical reactions significantly affects the first discharge capacity and capacity retention during cycling, highlighting the critical role of this interface in determining the performance and lifespan of batteries. Experimentally, distinguishing these two types of reactions from each other is a challenging task, as buried interfacial reactions are complex and challenging to be characterized. By constructing the phase equilibrium between cathodes and SSEs, we can get a comprehensive understanding of the interfacial reactions, and thus gain insight into the failure mechanism of the interface. We systematically analyzed the chemical reaction between SSEs and cathodes at the fully/half-lithiated state of cathodes, as well as electrochemical reactions at the applied chemical potential of μ_{Li} at the fully ($\mu_{Li}^{open,F}$) and half ($\mu_{Li}^{open,H}$) lithiated states of cathodes (Fig. 2, and the specific values of $\mu_{Li}^{open,F}/\mu_{Li}^{open,H}$ are shown in Fig S2, ESI†). It shows a general trend that the reactivity of cathodes with SSEs depends on the delithiated state of cathodes, and the higher the delithiated state, the stronger the reactivity. For example, the energy of the chemical reaction of $Li_{0.5}CoO_2$/LPS is 153 meV per atom higher than that of $LiCoO_2$/LPS. In general, most cathodes exhibit high chemical reactivity with SSEs with reaction energies of $\sim$310–586 and $\sim$420–769 meV per atom in the fully and half lithiated states of cathodes (Fig. 2(a) and (c)), respectively. The high reactivity originates from the big difference in the chemical potential of S/O in the cathode and SSEs at the interface, leading to the ion mutual diffusion and the formation of an interphase layer containing PO_4^{3-}, SO_4^{2-}, M_xS_y (M: Mn, Ni, Co), *etc.* $LiFePO_4$ shows better chemical stability with all sulfide solid electrolytes, and its reaction energy ($\sim$242 meV per atom) is almost one-third of other cathodes/SSE interfaces, which can be attributed to that the P ion possesses a similar anionic environment in PO_4^{3-} to that of PS_4^{3-} in the SSE. This trend is also applicable to other polyanionic cathodes, such as $LiCoPO_4$, $LiNiPO_4$, $LiMnPO_4$, *etc.*, shown in Fig. S3 (ESI†).

It is worth noting that the electrochemical reaction energy is much higher than that of the chemical reaction in both the

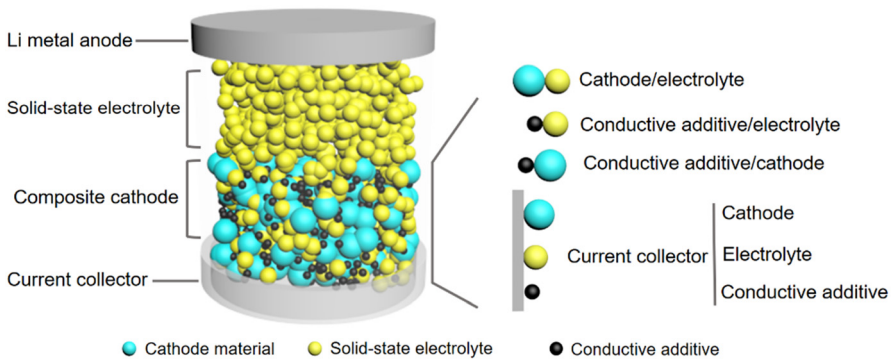

Fig. 1 Schematic illustration of various interfaces in the composite cathode of all solid-state batteries without coating.

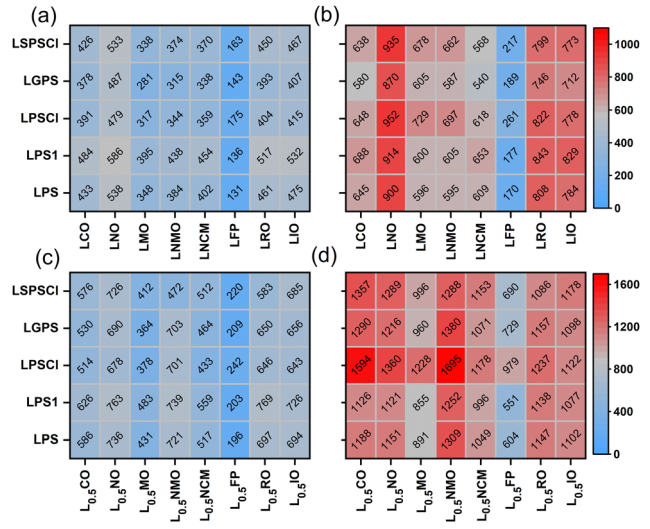

Fig. 2 Chemical and electrochemical compatibility between common cathodes and SSEs with the largest magnitude of chemical and electrochemical reaction energies ($-\Delta E_{\mathrm{D,mutual}}$ and $-\Delta E^{\varnothing}_{\mathrm{D,mutual}}$) of the cathodes/SSE interface in meV per atom. Chemical reaction energy in the fully (a) and half lithiated states of cathodes (c). Electrochemical reaction energy at the chemical potential of μ_{Li} in the fully ($\mu_{\mathrm{Li}}^{\mathrm{open,F}}$) (b) and half ($\mu_{\mathrm{Li}}^{\mathrm{open,H}}$) lithiated states of cathodes (d), respectively. Each cell is assigned a color from blue to red according to the color bar on the right, with the dark blue color denoting low reaction energy and the dark red color denoting high reaction energy, the specific value of energy is listed in each cell. Abbreviations, LCO: $LiCoO_2$, LNO: $LiNiO_2$, LMO: $LiMn_2O_4$, LNMO: $LiNi_{0.5}Mn_{1.5}O_4$, LNCM: $LiNi_{0.33}Mn_{0.33}Co_{0.33}O_2$, LFP: $LiFePO_4$, LRO: Li_2RuO_3, LIO: Li_2IrO_3, LPS: Li_3PS_4, LPS1: $Li_7P_3S_{11}$, LPSCl: Li_6PS_5Cl, LGPS: $Li_{10}Ge(PS_6)_2$, and LSPSCl: $Li_{9.54}Si_{1.74}P_{1.44}S_{11.7}Cl_{0.3}$.

fully and half lithiated states (Fig. 2(a)–(d)) and increases greatly with the increase of applied voltage. This suggests that the electrochemical reaction exhibits a significantly stronger driving force, thus dominating the interfacial reaction between cathodes and SSEs. For example, the electrochemical reaction energy of $L_{0.5}$NMO/LPSCl reaches 1695 meV per atom, which is 998 meV per atom higher than that of LNMO/LPSCl (697 meV per atom) and 994 meV per atom higher than the chemical reaction energy of $L_{0.5}$NMO/LPSCl (701 meV per atom). Additionally, $Li_{0.5}FePO_4$ also exhibits high electrochemical reactivity with SSEs with an energy of 551–979 meV per atom. Our calculation results are well consistent with the experimental results. It shows that the XPS results of S 2p and P 2p from SSEs show no significant difference before and after mixing with cathode materials during the composite preparation stage, which indicates that the accumulation of interphases resulting from chemical reactions between the SSEs and cathode is not visible. However, the content of the oxidized S and P species increase obviously after the first cycle and gradually increases in the subsequent cycling, indicating a continuous interfacial electrochemical reaction under the applied voltage (2.7–4.3 V).[53,58]

Since the interfacial reactions in composite cathodes occur simultaneously, it is necessary to get more detailed insight to understand the interfacial degradation mechanisms at different applied voltages. The percentage of mutual reaction energy of the chemical/electrochemical reaction between the cathode and the electrolyte and the electrochemical self-decomposition of SSEs are calculated in both the fully and half lithiated states of cathodes shown in Fig. 3. It can effectively reflect the difficulty of each part of interfacial reactions in the composite cathode. In the fully lithiated state of cathodes, the chemical and electrochemical reaction energy of the cathode/electrolyte accounts for more than 90%, suggesting that the interfacial deterioration of the composite cathode mainly occurs between the cathode active material and the electrolyte. However, for high voltage cathode LNMO, the oxidation of SSEs has already occurred at the applied chemical potential of $\mu_{\mathrm{Li}}^{\mathrm{open,F}}$, as the applied voltage exceeds the intrinsic stability windows of SSEs, resulting in a more severe parasitic reaction. It is well

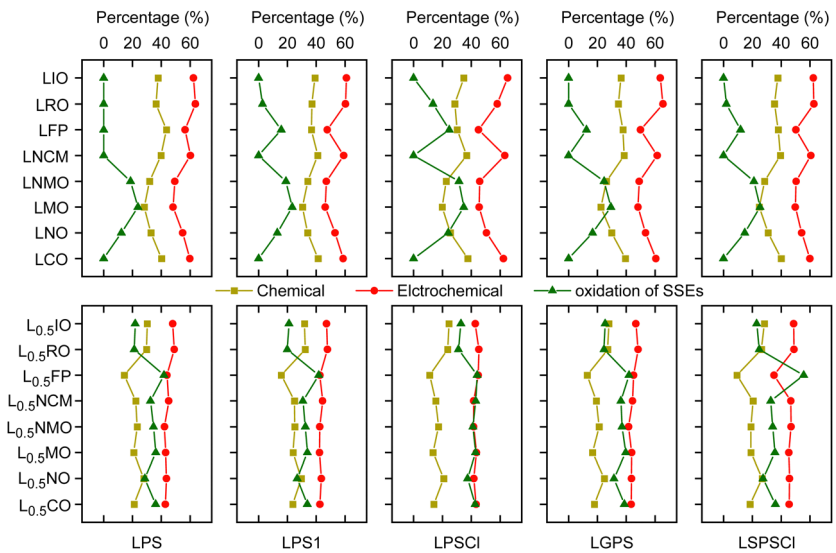

Fig. 3 Percentage of energy of mutual chemical/electrochemical reactions between cathodes and SSEs and the electrochemical self-decomposition of SSEs in the fully (top) and half (bottom) lithiated states of cathodes.

consistent with the experimental result that the discharge capacity of Li–In/LGPS/LNMO cell decreases from 80 mA h g^{-1} to 57 mA h g^{-1} in the first ten cycles and the impendence increase greatly.[59] In the half lithiated state of cathodes, the electrolyte undergoes severe oxidative decomposition leading to a high decomposition energy percentage (30%∼), which is higher than that of the chemical reaction and even close to that of the electrochemical reaction between the cathodes and the electrolytes. Therefore, the oxidation of electrolytes at high voltages is also an important aspect of the interfacial deterioration during voltage cycling. The oxidation of SSEs forms products with a low Li content and degrades the bulk structure, thereby reducing the Li-ion conduction of the composite cathode. It can be evidenced that the bulk and grain boundary resistance of β-Li_3PS_4 gradually increases with the applied voltage increase in the range of 3.0–3.6 V *vs.* Li/In.[58] Although the oxidation of SSEs at the electronically conductive additive and current collector surface is unavoidable during the first several cycles, it generally leads to the formation of an electronically insulating and thin passivated interphase consisting of oxidation products such as S, P_2S_7, *etc.* However, the electrochemical and chemical reaction between the cathode and the SSE directly leads to the capacity loss, and the driving force of the former is almost more than twice higher than that of the latter in both the fully and half lithiated states of the cathode. More seriously, the continuous occurrence of these reactions poses a significant challenge to achieving the long-term cyclability of ASSBs.

Electronic conductivity of the interphase layer

For electrochemical parasitic reactions to occur between the cathode and the electrolyte, it is a prerequisite that the interphase layer possesses adequate electronic conductivity. Hence, it is essential to understand the phases formed at the interface and their electronic conductivity. Therefore, the phase equilibria between SSEs and cathodes are systematically analyzed. For example, all possible phase equilibria of the chemical and electrochemical reactions between LPS and LCO in the fully/half-lithiated state of LCO, as well as at the applied voltages (corresponding to $\mu_{Li}^{open,F}$ and $\mu_{Li}^{open,H}$), are presented in Table S2 (ESI†), and the band gap of each product is listed in Table S3 (ESI†). Li_2SO_4 and Li_3PO_4, as the most common species, can be formed through the chemical/electrochemical reactions between LPS and LCO. Their existences are widely identified by the XPS spectra of S 2p (166–168 eV), P 2p (133 eV) and O 2p (531.1 eV) and are considered as the beneficial species that can passivate the interphase.[21,24,53,60 70] In the phase equilibrium, various types of transition metal sulfides (Co_xS_y) are formed, such as CoS_2, Co_3S_4, and Co_9S_8. Experimentally, their existence also has been identified by the XPS results of the 2p signal of transition metal (TM), Raman spectra, ToF-SIMS and XRD results.[31,53,63,64,71] All these transition metal sulfides possess zero Kohn–Sham band gaps and exhibit electronic conductivity.[15,72] Their distribution in the interphase layer offers the electronically conductive network, leading to a continuous electrochemical reaction between SSEs and cathodes and the thickening of interphase layers, thereby exacerbating the cycling performance. Herein, the percentage of molar fraction (f) of electronically conductive phases in all interphases formed at the interface was calculated to evaluate the electronic conductivity of the interphase layer and the feasibility of the electrochemical reaction. The higher f suggests the better electronic conductivity of the interphase layer and the higher feasibility of the electrochemical reaction between the cathodes and SSEs.

Fig. 4(a) shows a cross comparison of the percentage of the molar fraction of electronically conductive phases formed between cathodes/coatings and SSEs. The values vary greatly (11.2–43.9) when cathodes are matched with different SSEs (horizontal), as well as SSEs are matched with different cathodes (vertical). It is worthwhile mentioning that LPSCl possesses the smallest f value compared to other SSEs (LPS, LPS1, LGPS and LSPSCl). This suggests that the interphase layer between LPSCl/cathodes would be more passivated. The f value of LNCM/SSEs follows the order: LPSCl < LSPSCl < $Li_7P_3S_{11}$ < LGPS < Li_3PS_4. This trend agrees well with our experimental results that compared with LPS and LGPS, NCM coupled with LPSCl exhibits the highest initial discharge capacity and the best cycling performance at 0.3C, as shown in Fig. S4 (ESI†). Different from other SSEs ($Li_7P_3S_{11}$, LGPS and Li_3PS_4), plenty of LiCl can be formed through the chemical reaction between the cathode and LPSCl in the fully/half lithiated states and the electrochemical reaction at the applied chemical potential of $\mu_{Li}^{open,F}$. Additionally, Cl-contained species such as SCl, $CoPO_4Cl$ and $POCl_3$ will be formed by the electrochemical reaction at the applied chemical potential of $\mu_{Li}^{open,H}$ (Table S4, ESI†). These species with large band gaps as electronic insulators could effectively decrease the f of the interphase layer and passivate the interphase. Their existence has been evidenced by the XPS spectra of Cl 2p (198.5 eV and 200.2 eV) and ToF-SIMS.[63,73,74] For vertical comparison, the f value of LPSCl/cathodes follows the order of LRO (11.9) < LIO (13.1) < LNO (14.7) < LCO (16.4) < LNCM (25.1) < LMO (29.0) < LNMO (29.2). For the interphase layer with a high f value, the electrochemical parasitic reactions are feasible to take place at the cathode/electrolyte interface, as the composite cathode composed of LGPS and 16.3% carbon (the percentage of the molar fraction corresponds to the weight ratio of LGPS to carbon is 75 : 25) can be successfully charged and discharged with considerable capacity.[55,56] Notably, the LRO/LPSCl interphase with the smallest f among all combination of cathodes and SSEs would be favorable for the formation of a thin and passivating interphase layer. Our previous work has demonstrated that the uncoated LRO coupled with LPSCl exhibits excellent cycling performance (90% capacity retention after 1000 cycles), benefiting from the passivated interphase layer.[75] To further demonstrate the reliability of our calculation results, we also made a systematic comparison of the electrochemical performance of the common cathodes in combination with different types of SSEs (Table S5, ESI†). Its shows that the discharge capacity and capacity retention of cathodes coupled with LPSCl/LGPS/LPS also agrees well with our calculation results.

Furthermore, extending the same procedure to study the LiPON/LNMO interphase layer shows that the f value is

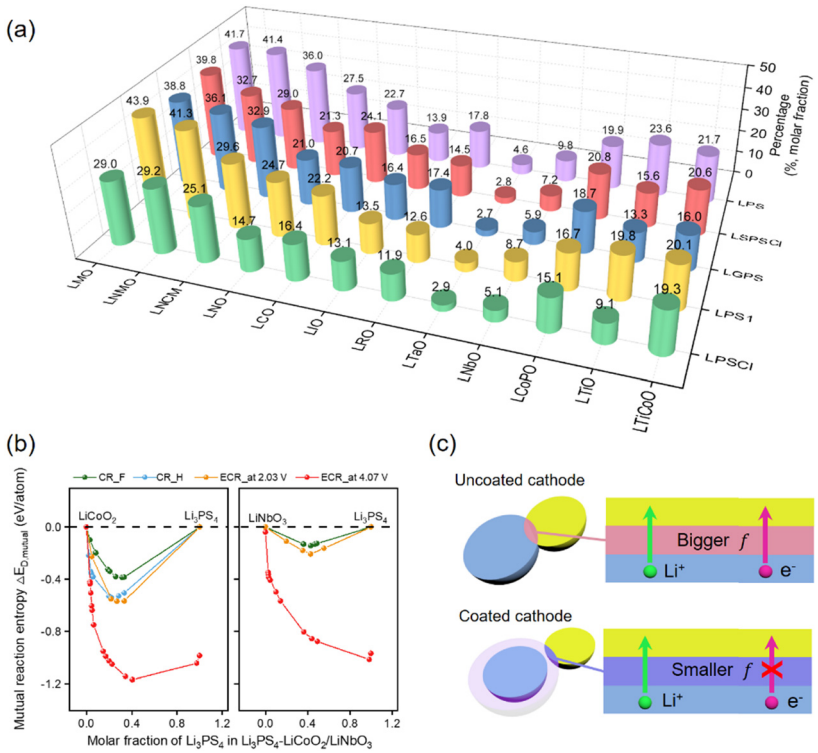

Fig. 4 (a) Percentage of the molar fraction of the phases with the Kohn–Sham band gap smaller than 0.5 eV in all interphases formed by the interfacial reactions between cathodes and SSEs. (b) Calculated chemical/electrochemical reaction energy between Li_3PS_4 and $LiCoO_2$/$LiNbO_3$ as a function of the mixing ratio of Li_3PS_4 in meV per atom. (c) Schematic diagram of the different types of interphase layers. Abbreviation: CR_F/H: chemical reaction in the fully/half-lithiated state of LCO, ECR: electrochemical reaction, LCO: $LiCoO_2$, LNO: $LiNiO_2$, LMO: $LiMn_2O_4$, LNMO: $LiNi_{0.5}Mn_{1.5}O_4$, LNCM: $LiNi_{0.33}Mn_{0.33}Co_{0.33}O_2$, LRO: Li_2RuO_3, LIO: Li_2IrO_3, LTaO: Li_7TaO_6, LNbO: $LiNbO_3$, LCoPO: $LiCoPO_4$, LTiO: $Li_4Ti_5O_{12}$, LTiCoO: $Li_2Ti_3CoO_8$, LPS: Li_3PS_4, LPS1: $Li_7P_3S_{11}$, LPSCl: Li_6PS_5Cl, LGPS: $Li_{10}Ge(PS_6)_2$, and LSPSCl: $Li_{9.54}Si_{1.74}P_{1.44}S_{11.7}Cl_{0.3}$.

relatively small with an average value of 9.4% over the voltage range of 3.0–5.0 V (Fig. S5, ESI†). This suggests that the formed interphases could effectively passivate the interphase. Our calculation results well explain that the Li/LiPON/LNMO cell can maintain 90% capacity retention after 10 000 cycles even at a high operating voltage (3.5–5.1 V) far beyond the intrinsic electrochemical window of the electrolyte (0.68–2.64 V), which is the best cycling stability reported for ASSBs so far.[33] This further confirms the reliability and universality of our calculation method.

Coating is a common and effective approach to mitigate interfacial reactions and improve the cycling performance of ASSBs, especially in SSE systems. For example, the initial discharge capacity of NCM622 can be enhanced to 180 mA h g^{-1} from 161 mA h g^{-1} and the capacity retention can be improved from 53% to 85% after 50 cycles by introducing the $LiNbO_3$ coating layer.[69] Once the coating is applied, two interfaces are simultaneously introduced: cathode/coating and coating/SSE interfaces. Most of the coatings show good chemical compatibility with both cathodes and SSEs with smaller chemical reaction energy, thereby converting the highly reactive interface into two more inert interfaces, as shown in Fig. S6 (ESI†). However, the chemical/electrochemical reactions between the coatings and SSEs may also be thermodynamically favorable, and thus the properties of the interphase layer between the coating and SSEs should be carefully considered. The species, such as Li_2SO_4, Li_3PO_4, *etc.*, can also be detected due to the interfacial reaction but the content is reduced after the coating process.[19,24,66,67,69] Notably, the driving force of the electrochemical reaction of $LiNbO_3$/Li_3PS_4 is almost equivalent to that of $Li_{0.5}CoO_2$/Li_3PS_4 at 4.07 V, as shown in Fig. 4(b). Hence, if the electronically conductive network can be formed within the interphase layer, a severe electrochemical reaction would occur at the coating/SSE interface. However, the *f* value of the interphase layer of $LiNbO_3$/Li_3PS_4 is relatively low (9.8%), which is close to that of LiPON/LNMO (9.4%). It effectively passivates the interphase and facilitates the formation of a passivated interphase layer with low resistance. Surprisingly, Li_7TaO_6 has the smallest *f* value (2.7–4.6%), suggesting that it would be a preferred candidate as a coating in sulfide-based ASSBs. It has been demonstrated that the cathode composed of Li_7TaO_6@NCM811 and LPSCl can be cycled for 5650 cycles with a capacity retention of 61.1% at 1.516 mA cm^{-2}.[76]

However, the current state of development of coatings for cathode/SSE interfaces is heavily reliant on trial-and-error approaches. It should be noted that not all coatings are capable of supporting ASSBs to achieve long-term cycling. Common coatings such as $Li_2Ti_3CoO_8$, $Li_4Ti_5O_{12}$ and $LiCoPO_4$ have been explored to modify the cathode/SSE interfaces. When combined with different SSEs, the *f* value is lower than that

of cathode/SSEs, but is still much higher than that of $LiNbO_3$/SSEs, as shown in the right-hand side of Fig. 4(a). Experimentally, cathodes coated with materials containing Ti and Co demonstrate enhanced cycling stability compared with the uncoated cathodes. However, achieving the long-term cycling performance of ASSBs still remains a challenge.[77] In general, the interfacial reaction between most of the cathodes and SSEs forms the interphase layers with high f values, also known as mixed ionic and electronic conductors (MIECs), which can lead to continuous electrochemical parasitic reactions during cycling and degrade the cyclability of ASSBs. The f value can be effectively reduced by introducing a suitable coating, and thus passivating the interphase (Fig. 4(c)). However, the available options for selecting preferable coatings are still limited, and there is an urgent need for developing guidelines to engineer suitable coatings.

Kohn–Sham band gap of ternary sulfides

As analysed above, a large amount of electronically conducting M_xS_y formed at the interface takes the main responsibility for the high electronic conductivity of the interphase layer, which should be avoided during the selection of coatings. The band gaps of binary sulfides (M_xS_y) are counted as shown in Fig. 5. The elements that make up M_xS_y span the entire periodic table, with different band gaps indicated by the color bar. Redder colors correspond to smaller Kohn–Sham band gaps, while bluer colors correspond to larger ones. It is found that the M_xS_y containing 3d transition metals, such as Ti, V, Mn, Fe, Co, Ni, Cu, *etc.*, possess zero Kohn–Sham band gaps, meaning that these binary sulfides are electronically conductive. The binary sulfides of the key elements (Mn, Co, Ni, and Fe) constituting common cathodes are the main source of electronic conductivity in the interphase layers, providing an electronically conductive network. Different from the 3d transition metal, the stable Ta/Nb containing compounds possess the high oxidation state of Ta^{5+} and Nb^{5+}, resulting in NbS_3 and TaS_3 being the only binary transition metal sulfides in the phase equilibrium between Nb/Ta-containing compounds and SSEs, and according to the principle of element conservation, forming high sulfur-containing binary transition metal sulfide is not conducive to the formation of a high f interphase layer. Therefore, the rational selection of coatings should place emphasis on the electronic conductivity of the interphase layer formed at the coating/SSE interface, which can facilitate the formation of a stable and thin passivating layer.

High-throughput screening of coatings

High-throughput screening is an efficient and economical approach to finding new functional coatings by filtering candidates based on specific properties. Excellent works have been conducted using HTS to screen cathode coatings for liquid electrolytes, oxide-based solid electrolytes, and SSE systems, taking into account the chemical and electrochemical stability of the coatings with respect to the electrolyte and the cathode.[37,48–50] Considering the critical role of the electron/ion conductive properties in the formation of compatible interphases with high stability and low resistance, we have proposed a specific workflow to screen the coatings that can form a passivated interphase layer between coatings and SSEs, thus effectively inhibiting the interface reactions (Fig. 6(a)). 17 082 Li-containing compounds, obtained from Material project,[78–80] are considered as the candidates for coatings. During the screening process, we carefully considered the following aspects.

(I) coatings used to stabilize SSEs against oxidation, must be electronically insulating. Otherwise, SSEs would be exposed to the applied high voltage at the coating/SSE interface. The band gap obtained from DFT calculations is considered as the first screening criterion for the electronic conductivity of coatings. It is set to be larger than 0.5 eV to exclude the materials that are electronically conductive. 10734 compounds satisfy the first filter and then are further evaluated for their phase stability.

(II) to achieve long-term cyclability in ASSBs, it is preferable for coatings to possess the capability to sustain their phase stability without decomposing into other phases during cycling. Herein, we use the energy convex hull <5 meV per atom to evaluate whether the specific compound would decompose into other phases during the battery operation. After this round of screening, 1195 compounds are screened out.

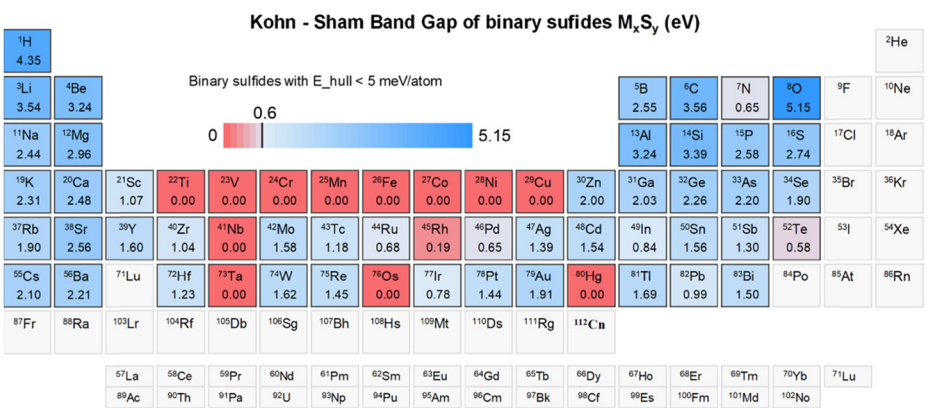

Fig. 5 The Kohn–Sham band gap of binary sulfides throughout the whole Periodic Table. The specific values of M_xS_y of each element are listed in Fig. S7 (ESI†). The redder the color where the element is, the smaller the band gap, while the blue color corresponds to an opposite trend.

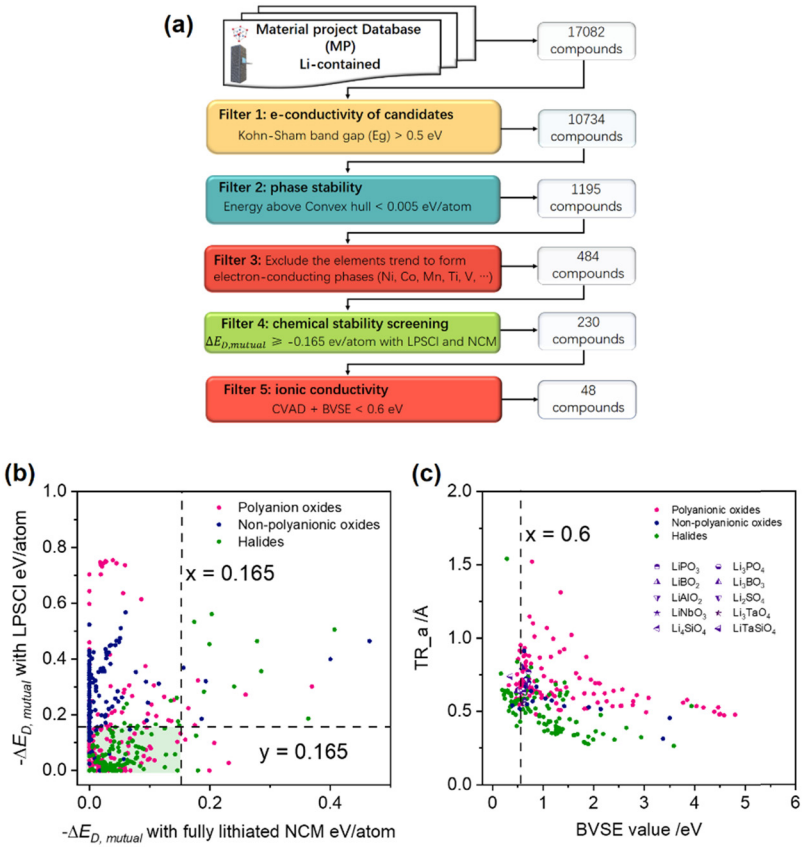

Fig. 6 (a) The flowchart of screening the coatings, (b) chemical reaction energy ($-\Delta E_{\mathrm{D,mutual}}$) with Li_6PS_5Cl (LPSCl) and fully lithiated $LiNi_{1/3}Co_{1/3}Mn_{1/3}O_2$ (NCM). Each material is represented by a dot in the graph, the red, dark blue, and green dots represent polyanionic oxides, non-polyanionic oxides and halides, respectively. (c) Threshold size along *a* direction (TR_a) and BVSE values of coatings that pass Filter 4. Common coatings used in experiments are highlighted by the specific symbols.

(III) to restrain the continuous electrochemical reactions between coatings and SSEs aroused by the electronic conductivity of the interphase upon cycling (decrease in the *f* value of the interphase layer), the compounds containing the elements that tend to form the electronically conductive species such as M_xS_y (M: Ti, V, Cr, Mn, Fe, Co, Ni and Cu) are excluded by filter 3, and 484 compounds pass this criterion.

(IV) except for maintaining the phase stability, coatings should also be stable with both SSEs and cathodes, simultaneously. To identify the chemical compatibility between the coatings with SSEs and cathodes, we use the chemical mixing reaction with the most negative reaction energy as an indicator to screen the coatings. To better understand the relationship between the composition and compatibility of compounds with the SSE and the cathode, the compounds are categorized into polyanionic oxide, non-polyanionic oxide and halide, depending on their anion chemistry. The polyanionic oxides refer to the oxides with a ''non-metal-oxygen cluster'' anion group, *e.g.*, MO_x^{y-} (M: metalloids, reactive nonmetals and halogens, as shown in Fig. S7, ESI†). Similarly, lithium containing metal oxides are categorized into non-polyanionic oxides (*i.e.*, $LiNbO_3$, $LiAlO_2$, Li_3TaO_4, Li_4GeO_4, *etc.*). Halides correspond to the compounds that only contain halogen elements as anions (such as F, Cl, Br, I).

Fig. 6(b) plots the chemical reaction energy ($-\Delta E_{\mathrm{D,mutual}}$) of the 484 candidates with LPSCl and $LiNi_{1/3}Co_{1/3}Mn_{1/3}O_2$ (NCM). Almost 90 percentage of non-polyanionic oxides exhibit good chemical compatibility with NCM ($\Delta E_{\mathrm{D,mutual}} \geq -50$ meV per atom); however, 74 percentage of them exhibit strong reactivity with LPSCl ($\Delta E_{\mathrm{D,mutual}} \leq -200$ meV per atom). This trend reminds us to be cautious in choosing metal oxides as cathode coatings for few of them can maintain stability with both cathodes and SSEs simultaneously. Polyanionic oxides also possess limited reactivity with NCM; however, the reactivity varies greatly with LPSCl. From the calculated reaction energies of halides (green dots in Fig. 6(b)), it can be inferred that halides are promising candidates possessing good compatibility with both SSEs and cathodes, simultaneously. Notably, 73.8% of halides exhibit limited reactivity with both LPSCl and NCM. The criterion for chemical reaction energy was set to be smaller than 165 meV per atom with both LPSCl and fully-lithiated NCM. This value is almost a quarter of the energy of the electrochemical reaction between common cathodes and SSEs (~600–952 meV per atom) in the fully-lithiated state. The candidates that passed the chemical stability screening will fall in the green shadow area in Fig. 6(b). Due to the high reactivity with LPSCl, only 14 non-polyanionic oxides pass filter 4, including commonly used coatings such as $LiNbO_3$, $LiAlO_2$,

Table 1 High-throughput screening results for coatings, the specific threshold size and Li ion diffusion energy barriers are listed in Table S7 (ESI)

Polyanionic oxides			Halides		Non-polyanionic oxides
Borates	Phosphates	Silicates	Fluorides	Chlorides	
Li_3BO_3	Li_3PO_4	$LiTaSiO_5$	K_2LiAlF_6	$LiCsCl_2$	Li_3NbO_4
$Li_3Sc(BO_3)_2$	$Li_3In_2(PO_4)_3$	Li_2ZnSiO_4	Li_2BeF_4	Li_3InCl_6	Li_5TaO_5
$Li_3Bi(BO_3)_2$	$LiBi(PO_3)_4$	$Li_4Al_3Si_3O_{12}Cl$	Li_2SiF_6	$LiAlCl_4$	
$Li_6Nd(BO_3)_3$	$Li_3Sc_2(PO_4)_3$	Sulfate	Li_3CrF_6	$LiGdCl_4$	
$Li_6Y(BO_3)_3$	$LiZr_2(PO_4)_3$	$Li_2Mg_2(SO_4)_3$	Li_3ScF_6	Bromides	
$Li_2Al(BO_2)_5$	$Li_4P_2O_7$		Li_4ZrF_8	$LiRbBr_2$	
Li_2AlBO_4	$LiInP_2O_7$		$LiBF_4$	Li_3ErBr_6	
$Li_6B_4O_9$	$LiScP_2O_7$		$Li_3Na_3Al_2F_{12}$	$LiGaBr_4$	
$Li_{10}B_{14}O_{25}Cl_2$	$Li_4Be_3P_3O_{12}Cl$		$Li_3Na_3Cr_2F_{12}$	Iodides	
$Li_2B_3O_4F_3$	$Li_4Be_3P_3O_{12}Br$		$Li_3Na_3Sc_2F_{12}$	$LiAuI_4$	
$Li_4B_7O_{12}Cl$			$Li_2RbBe_2F_7$	$LiGaI_4$	
				$LiInI_4$	

Li_2ZrO_3, *etc.* Polyanionic oxides such as Li_3BO_3, Li_3PO_4, Li_2SO_4, and Li_4SiO_4 are also located in the green shaded area, indicating the reasonability of our screening scheme.

(V) the effective conduction of ions through the electrode/SSE interface is crucial for minimizing interfacial resistance and promoting efficient ionic transport across the interphase.[18,24,67,81,82] Careful consideration should be given to screening coatings that possess fast ionic diffusion. Li-ion conductivity of coatings is also considered by analyzing the size of diffusion threshold and diffusion barrier energy (E_a) using CAVD[83,84] and BVSE[85,86] calculations. A suitable percolation radius is critical to the crystal structure to achieve fast ion conduction, and its size further influences the migration energy barrier.[87] Fig. 6(c) shows the relationship between the threshold (TR) size along *a* direction and the migration energy barrier of the candidates meeting the chemical compatibility screening. The threshold sizes along the *b* and *c* directions are shown in Fig. S8 (ESI†). The common coatings are marked in the graph and gathered within the area: $0.58 \leq$ TR_a ≤ 0.77 Å and $0.62 \leq E_a \leq 0.75$ eV. It is worth mentioning that the threshold sizes of selected polyanionic and non-polyanionic oxides are greater than 0.5 Å. This greatly satisfies the percolation radius distribution of fast oxide ionic conductors, such as $Li_{14}Zn(GeO_4)_4$: 0.54 Å, $Li_7La_3Zr_2O_{12}$: 0.62 Å, and $Li_{1.2}Al_{0.2}Ge_{0.2}Ti_{1.6}(PO_4)_3$: 0.72 Å.[88] The diffusion energy barrier is an effective descriptor for ion diffusivity. Although the DFT calculations can obtain high precision E_a, it is not suitable for high-throughput screening due to the expensive cost. In this work, we use the BVSE method to calculate the Li-ion diffusion energy barrier of 230 candidates, which are used for down-selection. The energy barrier filter was set to be $E_a \leq 0.6$ eV, the region to the left of the dotted line in the graph. Li_2ZrO_3, $LiPO_3$, $LiAlO_2$, $LiNbO_3$, and Li_2SO_4 coatings used in the experiment are excluded for their high diffusion energy barriers.

The summary of the numbers and rates for the three categories that pass each of the filters is presented in Fig. S9 and Table S6 (ESI†). Due to the different anionic chemistry, three categories exhibit different sensitivities to the same filter. For example, excluding the candidates that are prone to form the electronically conductive phases M_xS_y, most of the 3d-transition-metals are eliminated. These 3d-transition metals are the key elements constituting the polyanionic and non-polyanionic oxides. As a result, 203 polyanionic oxides (34.6%) and 151 non-polyanionic oxides (40.1%) satisfy filter 3, and the pass rates are smaller than that of halide (56.3%). Although non-polyanionic oxides exhibit good stability with NCM (Filter 4), the high reactivity with LPSCl results in only 14 compounds are screened out with the lowest pass rate (9.3%, Table S6, ESI†). Finally, 48 candidates pass the Li ion conductivity screening (Filter 5) (polyanionic oxides: 25, non-polyanionic oxides: 2, and halides: 21).

The candidates that pass all filters are listed in Table 1. Based on the screening results, each category is further divided into several sub-groups according to their anions, *i.e.*, polyanionic oxides including borates, phosphates, silicates, and sulfates. $LiTaSiO_4$ is proven as a fast Li ion conductor and synthesized by Mo, *et al.*[88] $Li_3Sc(BO_3)_2$, as a NASICON type conductor, possesses a low Li ion diffusion energy barrier of 0.29 ± 0.92 eV.[89] Halide solid electrolytes, such as Li_3InCl_6,[90,91] Li_3ErBr_6,[92] and $LiAlCl_4$,[93,94] are also selected by our screening scheme. The selected coatings not only exhibit good chemical compatibility with both the solid electrolyte and the cathode but also can effectively reduce the electronic conductivity of the interphase layer, thus inhibiting the interfacial electrochemical parasitic reactions. Moreover, they also possess high Li-ionic conductivity, indicating great potential for improving the interface compatibility and enhancing the Li-ion conduction at the interface. Plenty of fast Li ion conductors appear in our screening results further verifying the reasonability of our screening scheme.

Conclusions

In this study, we systematically investigated the interfacial reactions that occur in sulfide solid electrolyte (SSE) based composite cathodes, including both chemical and electrochemical reactions between the cathodes and SSEs, as well as the electrochemical self-decomposition of the electrolyte. The composition and electron-conducting properties of the resulting interphases were also carefully analyzed. It was found that the driving force of the electrochemical reaction between the

cathode and the electrolyte is approximately two times greater than that of the chemical reaction in both the fully and half-lithiated states of the cathode, indicating that the electrochemical reaction plays a dominant role in the interfacial reactions during cycling. The reactions between the cathode and SSEs will lead to the generation of transition metal sulfides (M_xS_y) with a zero band-gap, resulting in the formation of mixed ionically and electronically conducting interphases. The electronic conductivity of the interphase layer plays a crucial role in driving the continuous interfacial reaction in the composite cathodes, which is an essential aspect of interphase compatibility between cathodes and SSEs during long-term cycling. We proposed the percentage of molar fraction (f) of electronically conductive species in all products as a key factor to indicate the electrochemical stability of the interface for the first time. An interphase layer with a smaller f should be preferred as it can effectively inhibit the continuous electrochemical reactions at the interface, which suppress the further growth of the interphase layer, thus facilitating the formation of a thin and passivating interphase layer. The interphase layer formed with LPSCl possesses the smallest f, thus exhibiting higher interfacial stability and superior cycling stability among the interphase formed between the popular oxide cathodes with sulfide solid electrolytes (Li_3PS_4 and LGPS). Considering the rational selection of coating materials to realize the desired interfacial properties, a specific high-throughput screening scheme to filter functional coating materials has been proposed. The electronic and ionic conductivity, phase stability, electronic conductivity of the formed interphase layer, and chemical stability (with both cathodes and SSEs) were used as screening filters. Forty-eight coating materials with the desired properties are screened out, exhibiting good chemical stability with both cathodes and SSEs and possessing high Li conductivity. The regulation of the interfacial composition and properties plays an essential role in achieving desired electrochemical performance in ASSBs. Our calculations provide valuable guidance for rational coupling of the cathodes and SSEs, and versatile criteria for the selection of the interfacial coating materials to realize the desired interfacial properties, facilitating the realization of high performance ASSBs with long-term cycling.

Author contributions

F. R. conceived and finished the calculations and original draft. Z. L. assembled the ASSBs and performed the electrochemical measurements. W. G. Z. and W. H. Z. attended the revision of the manuscript. Z. G. & Y. Y. edited and finalized the manuscript. All authors discussed the results and commented on the manuscript.

Conflicts of interest

There are no conflicts to declare.

Acknowledgements

This work was supported by the National Natural Science Foundation of China (grants no. 22261160570, 21935009 and 22279108) and the National Key R&D Program of China (grant no. 2021YFB2401800).

Notes and references

1 L. Liu, J. Xu, S. Wang, F. Wu, H. Li and L. Chen, *eTransportation*, 2019, **1**, 100010.
2 Y. Zhu, J. C. Gonzalez-Rosillo, M. Balaish, Z. D. Hood, K. J. Kim and J. L. M. Rupp, *Nat. Rev. Mater.*, 2020, **6**, 313–331.
3 C. Wang, K. Fu, S. P. Kammampata, D. W. McOwen, A. J. Samson, L. Zhang, G. T. Hitz, A. M. Nolan, E. D. Wachsman, Y. Mo, V. Thangadurai and L. Hu, *Chem. Rev.*, 2020, **120**, 4257–4300.
4 J. C. Bachman, S. Muy, A. Grimaud, H. H. Chang, N. Pour, S. F. Lux, O. Paschos, F. Maglia, S. Lupart, P. Lamp, L. Giordano and Y. Shao-Horn, *Chem. Rev.*, 2016, **116**, 140–162.
5 J. Wu, S. Liu, F. Han, X. Yao and C. Wang, *Adv. Mater.*, 2021, **33**, e2000751.
6 C. Wang, J. Liang, Y. Zhao, M. Zheng, X. Li and X. Sun, *Energy Environ. Sci.*, 2021, **14**, 2577–2619.
7 K. H. Park, Q. Bai, D. H. Kim, D. Y. Oh, Y. Zhu, Y. Mo and Y. S. Jung, *Adv. Energy Mater.*, 2018, 8.
8 H. Kwak, S. Wang, J. Park, Y. Liu, K. T. Kim, Y. Choi, Y. Mo and Y. S. Jung, *ACS Energy Lett.*, 2022, **7**, 1776–1805.
9 J. Liang, X. Li, K. R. Adair and X. Sun, *Acc. Chem. Res.*, 2021, **54**, 1023–1033.
10 Z. Zou, Y. Li, Z. Lu, D. Wang, Y. Cui, B. Guo, Y. Li, X. Liang, J. Feng, H. Li, C. W. Nan, M. Armand, L. Chen, K. Xu and S. Shi, *Chem. Rev.*, 2020, **120**, 4169–4221.
11 F. Mizuno, A. Hayashi, K. Tadanaga and M. Tatsumisago, *Adv. Mater.*, 2005, **17**, 918–921.
12 N. Kamaya, K. Homma, Y. Yamakawa, M. Hirayama, R. Kanno, M. Yonemura, T. Kamiyama, Y. Kato, S. Hama, K. Kawamoto and A. Mitsui, *Nat. Mater.*, 2011, **10**, 682–686.
13 Y. Kato, S. Hori, T. Saito, K. Suzuki, M. Hirayama, A. Mitsui, M. Yonemura, H. Iba and R. Kanno, *Nat. Energy*, 2016, 1.
14 J. Haruyama, K. Sodeyama, L. Han, K. Takada and Y. Tateyama, *Chem. Mater.*, 2014, **26**, 4248–4255.
15 B. Gao, R. Jalem, Y. Ma and Y. Tateyama, *Chem. Mater.*, 2019, **32**, 85–96.
16 Y. Okuno, J. Haruyama and Y. Tateyama, *ACS Appl. Energy Mater.*, 2020, **3**, 11061–11072.
17 Y. Zhu, X. He and Y. Mo, *ACS Appl. Mater. Interfaces*, 2015, **7**, 23685–23693.
18 A. Sakuda, A. Hayashi and M. Tatsumisago, *Chem. Mater.*, 2010, **22**, 949–956.
19 X. Liu, B. Zheng, J. Zhao, W. Zhao, Z. Liang, Y. Su, C. Xie, K. Zhou, Y. Xiang, J. Zhu, H. Wang, G. Zhong, Z. Gong, J. Huang and Y. Yang, *Adv. Energy Mater.*, 2021, **11**, 2003583.
20 S. Randau, D. A. Weber, O. Kötz, R. Koerver, P. Braun, A. Weber, E. Ivers-Tiffée, T. Adermann, J. Kulisch,

W. G. Zeier, F. H. Richter and J. Janek, *Nat. Energy*, 2020, **5**, 259–270.
21 J. R. M. Auvergniot, A. Cassel, J. B. Ledeuil, V. Vialle, V. Seznec and R. M. Dedryvère, *Chem. Mater.*, 2017, **29**, 3883–3890.
22 S. Wang, W. Zhang, X. Chen, D. Das, R. Ruess, A. Gautam, F. Walther, S. Ohno, R. Koerver, Q. Zhang, W. G. Zeier, F. H. Richter, C. W. Nan and J. Janek, *Adv. Energy Mater.*, 2021, **11**, 2100654.
23 N. Ohta, K. Takada, I. Sakaguchi, L. Zhang, R. Ma, K. Fukuda, M. Osada and T. Sasaki, *Electrochem. Commun.*, 2007, **9**, 1486–1490.
24 W. Zhang, F. H. Richter, S. P. Culver, T. Leichtweiss, J. G. Lozano, C. Dietrich, P. G. Bruce, W. G. Zeier and J. Janek, *ACS Appl. Mater. Interfaces*, 2018, **10**, 22226–22236.
25 Y. Su, J. L. Hao, X. S. Liu and Y. Yang, *Batteries Supercaps*, 2023, **6**, e202200359.
26 Y. Sakurai, A. Sakuda, A. Hayashi and M. Tatsumisago, *Solid State Ionics*, 2011, **182**, 59–63.
27 B. Wang, J. Liu, Q. Sun, R. Li, T. K. Sham and X. Sun, *Nanotechnology*, 2014, **25**, 504007.
28 S. Yubuchi, Y. Ito, T. Matsuyama, A. Hayashi and M. Tatsumisago, *Solid State Ionics*, 2016, **285**, 79–82.
29 K. Takada, N. Ohta, L. Zhang, K. Fukuda, I. Sakaguchi, R. Ma, M. Osada and T. Sasaki, *Solid State Ionics*, 2008, **179**, 1333–1337.
30 K. Okada, N. Machida, M. Naito, T. Shigematsu, S. Ito, S. Fujiki, M. Nakano and Y. Aihara, *Solid State Ionics*, 2014, **255**, 120–127.
31 S. H. Jung, K. Oh, Y. J. Nam, D. Y. Oh, P. Brüner, K. Kang and Y. S. Jung, *Chem. Mater.*, 2018, **30**, 8190–8200.
32 A. M. Nolan, Y. Zhu, X. He, Q. Bai and Y. Mo, *Joule*, 2018, **2**, 2016–2046.
33 J. Li, C. Ma, M. Chi, C. Liang and N. J. Dudney, *Adv. Energy Mater.*, 2015, **5**, 1401408.
34 A. D. Sendek, Q. Yang, E. D. Cubuk, K.-A. N. Duerloo, Y. Cui and E. J. Reed, *Energy Environ. Sci.*, 2017, **10**, 306–320.
35 A. Jain, G. Hautier, C. J. Moore, S. Ping Ong, C. C. Fischer, T. Mueller, K. A. Persson and G. Ceder, *Comput. Mater. Sci.*, 2011, **50**, 2295–2310.
36 G. Hautier, A. Jain, S. P. Ong, B. Kang, C. Moore, R. Doe and G. Ceder, *Chem. Mater.*, 2011, **23**, 3495–3508.
37 A. M. Nolan, E. D. Wachsman and Y. Mo, *Energy Storage Mater.*, 2021, **4**, 571–580.
38 Y. Zhu and Y. Mo, *Angew. Chem., Int. Ed.*, 2020, **59**, 17472–17476.
39 V. Lacivita, Y. Wang, S.-H. Bo and G. Ceder, *J. Mater. Chem. A*, 2019, **7**, 8144–8155.
40 W. Fitzhugh, F. Wu, L. Ye, W. Deng, P. Qi and X. Li, *Adv. Energy Mater.*, 2019, **9**, 1900807.
41 Y. Zhu, X. He and Y. Mo, *Adv. Sci.*, 2017, **4**, 1600517.
42 H. Tang, Z. Deng, Z. Lin, Z. Wang, I.-H. Chu, C. Chen, Z. Zhu, C. Zheng and S. P. Ong, *Chem. Mater.*, 2017, **30**, 163–173.
43 Y. Zhu, X. He and Y. Mo, *J. Mater. Chem. A*, 2016, **4**, 3253–3266.
44 W. D. Richards, L. J. Miara, Y. Wang, J. C. Kim and G. Ceder, *Chem. Mater.*, 2015, **28**, 266–273.
45 S. Li, Z. Chen, W. Zhang, S. Li and F. Pan, *Nano Energy*, 2022, **102**, 107640.
46 B. Zhang, Z. Lin, L. W. Wang and F. Pan, *ACS Appl. Mater. Interfaces*, 2020, **12**, 6007–6014.
47 S. Yu, H. Park and D. J. Siegel, *ACS Appl. Mater. Interfaces*, 2019, **11**, 36607–36615.
48 Y. Xiao, L. J. Miara, Y. Wang and G. Ceder, *Joule*, 2019, **3**, 1252–1275.
49 M. Aykol, S. Kim, V. I. Hegde, D. Snydacker, Z. Lu, S. Hao, S. Kirklin, D. Morgan and C. Wolverton, *Nat. Commun.*, 2016, **7**, 13779.
50 A. M. Nolan, Y. Liu and Y. Mo, *ACS Energy Lett.*, 2019, **4**, 2444–2451.
51 A. Jain, S. P. Ong, W. Chen, B. Medasani, X. Qu, M. Kocher, M. Brafman, G. Petretto, G.-M. Rignanese, G. Hautier, D. Gunter and K. A. Persson, *Concurr. Comput. Pract. Exp.*, 2015, **27**, 5037–5059.
52 A. Banerjee, X. Wang, C. Fang, E. A. Wu and Y. S. Meng, *Chem. Rev.*, 2020, **120**, 6878–6933.
53 F. Walther, S. Randau, Y. Schneider, J. Sann, M. Rohnke, F. H. Richter, W. G. Zeier and J. Janek, *Chem. Mater.*, 2020, **32**, 6123–6136.
54 G. F. Dewald, S. Ohno, M. A. Kraft, R. Koerver, P. Till, N. M. Vargas-Barbosa, J. Janek and W. G. Zeier, *Chem. Mater.*, 2019, **31**, 8328–8337.
55 F. Han, T. Gao, Y. Zhu, K. J. Gaskell and C. Wang, *Adv. Mater.*, 2015, **27**, 3473–3483.
56 F. Han, Y. Zhu, X. He, Y. Mo and C. Wang, *Adv. Energy Mater.*, 2016, **6**, 1501590.
57 T. Swamy, X. Chen and Y. M. Chiang, *Chem. Mater.*, 2019, **31**, 707–713.
58 R. Koerver, I. Aygün, T. Leichtweiß, C. Dietrich, W. Zhang, J. O. Binder, P. Hartmann, W. G. Zeier and J. Janek, *Chem. Mater.*, 2017, **29**, 5574–5582.
59 G. Oh, M. Hirayama, O. Kwon, K. Suzuki and R. Kanno, *Chem. Mater.*, 2016, **28**, 2634–2640.
60 S. Deng, Q. Sun, M. Li, K. Adair, C. Yu, J. Li, W. Li, J. Fu, X. Li, R. Li, Y. Hu, N. Chen, H. Huang, L. Zhang, S. Zhao, S. Lu and X. Sun, *Energy Storage Mater.*, 2021, **35**, 661–668.
61 F. Zhao, Y. Zhao, J. Wang, Q. Sun, K. Adair, S. Zhang, J. Luo, J. Li, W. Li, Y. Sun, X. Li, J. Liang, C. Wang, R. Li, H. Huang, L. Zhang, S. Zhao, S. Lu and X. Sun, *Energy Storage Mater.*, 2020, **33**, 139–146.
62 G. Liu, Y. Lu, H. Wan, W. Weng, L. Cai, Z. Li, X. Que, H. Liu and X. Yao, *ACS Appl. Mater. Interfaces*, 2020, **12**, 28083–28090.
63 F. Walther, R. Koerver, T. Fuchs, S. Ohno, J. Sann, M. Rohnke, W. G. Zeier and J. Janek, *Chem. Mater.*, 2019, **31**, 3745–3755.
64 A. Banerjee, H. Tang, X. Wang, J. H. Cheng, H. Nguyen, M. Zhang, D. H. S. Tan, T. A. Wynn, E. A. Wu, J. M. Doux, T. Wu, L. Ma, G. E. Sterbinsky, M. S. D'Souza, S. P. Ong and Y. S. Meng, *ACS Appl. Mater. Interfaces*, 2019, **11**, 43138–43145.
65 J. Auvergniot, A. Cassel, D. Foix, V. Viallet, V. Seznec and R. Dedryvère, *Solid State Ionics*, 2017, **300**, 78–85.

66 C. Wang, S. Hwang, M. Jiang, J. Liang, Y. Sun, K. Adair, M. Zheng, S. Mukherjee, X. Li, R. Li, H. Huang, S. Zhao, L. Zhang, S. Lu, J. Wang, C. V. Singh, D. Su and X. Sun, *Adv. Energy Mater.*, 2021, **11**, 2100210.

67 S. Deng, X. Li, Z. Ren, W. Li, J. Luo, J. Liang, J. Liang, M. N. Banis, M. Li, Y. Zhao, X. Li, C. Wang, Y. Sun, Q. Sun, R. Li, Y. Hu, H. Huang, L. Zhang, S. Lu, J. Luo and X. Sun, *Energy Storage Mater.*, 2020, **27**, 117–123.

68 W. Zhang, T. Leichtweiss, S. P. Culver, R. Koerver, D. Das, D. A. Weber, W. G. Zeier and J. Janek, *ACS Appl. Mater. Interfaces*, 2017, **9**, 35888–35896.

69 F. Walther, F. Strauss, X. Wu, B. Mogwitz, J. Hertle, J. Sann, M. Rohnke, T. Brezesinski and J. Janek, *Chem. Mater.*, 2021, **33**, 2110–2125.

70 J. H. Teo, F. Strauss, F. Walther, Y. Ma, S. Payandeh, T. Scherer, M. Bianchini, J. Janek and T. Brezesinski, *Mater. Future*, 2022, **1**, 015102.

71 S. Wang, Y. Wu, T. Ma, L. Chen, H. Li and F. Wu, *ACS Nano*, 2022, **16**, 16158–16176.

72 M. H. Wu, W. J. Chou, J. S. Huang, D. B. Putungan and S. H. Lin, *Phys. Chem. Chem. Phys.*, 2019, **21**, 21561–21567.

73 S. K. Jung, H. Gwon, S. S. Lee, H. Kim, J. C. Lee, J. G. Chung, S. Y. Park, Y. Aihara and D. Im, *J. Mater. Chem. A*, 2019, **7**, 22967–22976.

74 J. Zhang, C. Zheng, L. Li, Y. Xia, H. Huang, Y. Gan, C. Liang, X. He, X. Tao and W. Zhang, *Adv. Energy Mater.*, 2019, 10.

75 Y. Q. Wu, K. Zhou, F. C. Ren, Y. Ha, Z. T. Liang, X. F. Zheng, Z. Y. Wang, W. Yang, M. J. Zhang, M. Z. Luo, C. Battaglia, W. L. Yang, L. Y. Zhu, Z. L. Gong and Y. Yang, *Energy Environ. Sci.*, 2022, **15**, 3470–3482.

76 J. Shi, Z. Ma, K. Han, Q. Wan, D. Wu, X. Qu and P. Li, *J. Mater. Chem. A*, 2022, **10**, 21336–21348.

77 C. W. Wang, F. C. Ren, Y. Zhou, P. F. Yan, X. D. Zhou, S. J. Zhang, W. Liu, W. D. Zhang, M. H. Zou, L. Y. Zeng, X. Y. Yao, L. Huang, J. T. Li and S. G. Sun, *Energy Environ. Sci.*, 2021, **14**, 437–450.

78 S. P. Ong, W. D. Richards, A. Jain, G. Hautier, M. Kocher, S. Cholia, D. Gunter, V. L. Chevrier, K. A. Persson and G. Ceder, *Comput. Mater. Sci.*, 2013, **68**, 314–319.

79 K. T. Schutt, H. E. Sauceda, P. J. Kindermans, A. Tkatchenko and K. R. Muller, *J. Chem. Phys.*, 2018, **148**, 241722.

80 A. Jain, J. Montoya, S. Dwaraknath, N. E. R. Zimmermann, J. Dagdelen, M. Horton, P. Huck, D. Winston, S. Cholia, S. P. Ong and K. Persson, *Handbook of Materials Modeling: Methods: Theory and Modeling*, 2020, pp.1751–1784.

81 N. Ohta, K. Takada, L. Zhang, R. Ma, M. Osada and T. Sasaki, *Adv. Mater.*, 2006, **18**, 2226–2229.

82 X. Li, Q. Sun, Z. Wang, D. Song, H. Zhang, X. Shi, C. Li, L. Zhang and L. Zhu, *J. Power Sources*, 2020, **456**, 227997.

83 B. He, A. Ye, S. Chi, P. Mi, Y. Ran, L. Zhang, X. Zou, B. Pu, Q. Zhao, Z. Zou, D. Wang, W. Zhang, J. Zhao, M. Avdeev and S. Shi, *Sci. Data*, 2020, **7**, 153.

84 B. He, S. Chi, A. Ye, P. Mi, L. Zhang, B. Pu, Z. Zou, Y. Ran, Q. Zhao, D. Wang, W. Zhang, J. Zhao, S. Adams, M. Avdeev and S. Shi, *Sci. Data*, 2020, **7**, 151.

85 I. D. Brown, *Chem. Rev.*, 2009, **109**, 6858–6919.

86 S. Adams, *Solid State Ionics*, 2000, **137**, 1351–1361.

87 L. Zhang, B. He, Q. Zhao, Z. Zou, S. Chi, P. Mi, A. Ye, Y. Li, D. Wang, M. Avdeev, S. Adams and S. Shi, *Adv. Funct. Mater.*, 2020, **30**, 2003087.

88 X. He, Q. Bai, Y. Liu, A. M. Nolan, C. Ling and Y. Mo, *Adv. Energy Mater.*, 2019, **9**, 1902078.

89 Y. Xiao, K. Jun, Y. Wang, L. J. Miara, Q. Tu and G. Ceder, *Adv. Energy Mater.*, 2021, **11**, 2101437.

90 X. Li, J. Liang, J. Luo, M. Norouzi Banis, C. Wang, W. Li, S. Deng, C. Yu, F. Zhao, Y. Hu, T. K. Sham, L. Zhang, S. Zhao, S. Lu, H. Huang, R. Li, K. R. Adair and X. Sun, *Energy Environ. Sci.*, 2019, **12**, 2665–2671.

91 W. Li, J. Liang, M. Li, K. R. Adair, X. Li, Y. Hu, Q. Xiao, R. Feng, R. Li, L. Zhang, S. Lu, H. Huang, S. Zhao, T. K. Sham and X. Sun, *Chem. Mater.*, 2020, **32**, 7019–7027.

92 R. Schlem, S. Muy, N. Prinz, A. Banik, Y. S. Horn, M. Zobel and W. G. Zeier, *Adv. Energy Mater.*, 2019, **10**, 1903719.

93 Y. Liu, S. Wang, A. M. Nolan, C. Ling and Y. Mo, *Adv. Energy Mater.*, 2020, **10**, 2002356.

94 N. F. González, N. Minafra, G. Dewald, H. Reardon, R. I. Smith, S. Adams, W. G. Zeier and D. H. Gregory, *ACS Mater. Lett.*, 2021, **3**, 652–657.